


## Orbital torque originating from orbital Hall effect in Zr

Riko Fukunaga<sup>1</sup>, Satoshi Haku<sup>1</sup>, Hiroki Hayashi<sup>1</sup>, and Kazuya Ando<sup>1,2,3,\*</sup><sup>1</sup>Department of Applied Physics and Physico-Informatics, Keio University, Yokohama 223-8522, Japan<sup>2</sup>Keio Institute of Pure and Applied Sciences, Keio University, Yokohama 223-8522, Japan<sup>3</sup>Center for Spintronics Research Network, Keio University, Yokohama 223-8522, Japan (Received 24 November 2022; revised 30 January 2023; accepted 1 March 2023; published 25 April 2023)

We investigate current-induced torques generated by Zr. We show that the generation efficiency of the current-induced torque increases with increasing the thickness of the Zr layer in Ni<sub>81</sub>Fe<sub>19</sub>/Zr and Ni/Zr bilayers, which indicates that the observed current-induced torque originates from the bulk of the Zr layer. We find that the sign of the current-induced torques is opposite to that expected from the spin Hall effect but is consistent with that expected from the orbital Hall effect in the Zr layer. Furthermore, we find that the torque efficiency increases with increasing the thickness of the ferromagnetic layer, which is consistent with the prediction of long-range orbital transport in ferromagnets. These observations demonstrate that the orbital Hall effect in the Zr layer is the main source of the current-induced torque. This finding highlights the important role of orbital transport in generating current-induced torques, advancing the understanding of angular momentum dynamics in solid-state devices with 4d transition metals.

DOI: [10.1103/PhysRevResearch.5.023054](https://doi.org/10.1103/PhysRevResearch.5.023054)

## I. INTRODUCTION

Since its discovery, the spin Hall effect (SHE) has played a key role in the exploration of the physics of spin currents and the development of spintronic devices [1,2]. The SHE generates a spin current from a charge current through spin-orbit coupling, allowing to transfer angular momentum from the crystal lattice to the electronic system. The angular momentum transfer triggered by the SHE is a major source of current-induced torques, which enable the electric manipulation of magnetization [3,4]. The manipulation of magnetization using the current-induced torque has been one of the central topics of spintronics.

In the angular momentum dynamics in solids, the orbital counterpart of the spin Hall effect, the orbital Hall effect (OHE), has been predicted to play an essential role [5–12]. The OHE is a phenomenon that generates an orbital current flowing perpendicular to an applied charge current. Recent experimental studies have suggested the presence of current-induced torques arising from the orbital Hall effect, orbital torques, in metallic devices [13–18]. Although the exploration of orbital transport is just beginning and further experimental studies are required to confirm the role of the OHE in generating the current-induced torque, these studies open a new direction for spintronics.

In this paper we investigate the orbital Hall contribution to the current-induced torque generated by Zr, which is one of the materials that have been suggested to generate the orbital

torque [13]. We find that the sign of the current-induced torque in Ni<sub>81</sub>Fe<sub>19</sub>/Zr and Ni/Zr bilayers is opposite to that expected from the SHE in the Zr layer. By changing the thickness  $t_{\text{Zr}}$  of the Zr layer, we show that the observed torque efficiency varies with  $t_{\text{Zr}}$ , even when  $t_{\text{Zr}}$  is clearly larger than the spin diffusion length of Zr. Furthermore, the torque efficiency increases with the ferromagnetic (FM) layer thickness, which demonstrates that spin currents are not responsible for the observed torque. We also find that the magnitude of the unconventional torque is stronger in the Ni/Zr bilayer than in the Ni<sub>81</sub>Fe<sub>19</sub>/Zr bilayer. These results are consistent with the prediction of the orbital torque generated by the OHE in the Zr layer.

## II. EXPERIMENTAL METHODS

We investigated the current-induced torques using the spin-torque ferromagnetic resonance (ST-FMR) for Ni/Zr and Ni<sub>81</sub>Fe<sub>19</sub>/Zr bilayers [see Fig. 1(a)]. The films were deposited on thermally oxidized Si substrates by the rf magnetron sputtering, where the base pressure was better than  $3 \times 10^{-6}$  Pa. During the sputtering, a linear shutter was used to vary the thickness of one layer, the Zr or Ni layer, in each substrate. The variation of the Zr(Ni) thickness across each device is 0.018 nm (0.036 nm). To avoid the oxidation of the films, the surface of the FM layer was covered by a 4-nm-thick SiO<sub>2</sub> capping layer, which was sputtered from a SiO<sub>2</sub> target in an Ar atmosphere. To characterize the microstructure of the Zr layer, we conducted x-ray diffraction (XRD) measurements on a Zr film, as shown in Fig. 1(b). The XRD pattern shows that the Zr film is hexagonal close-packed (hcp) structure.

For the ST-FMR measurements, the films were patterned into  $150 \mu\text{m} \times 10 \mu\text{m}$  stripes by photolithography and Ar ion-milling processes. On the edges of the strip, Au(100 nm)/Ti(2 nm) electrodes were sputtered and patterned by photolithography and lift-off processes to form a ground-

\*ando@appi.keio.ac.jp

Published by the American Physical Society under the terms of the Creative Commons Attribution 4.0 International license. Further distribution of this work must maintain attribution to the author(s) and the published article's title, journal citation, and DOI.

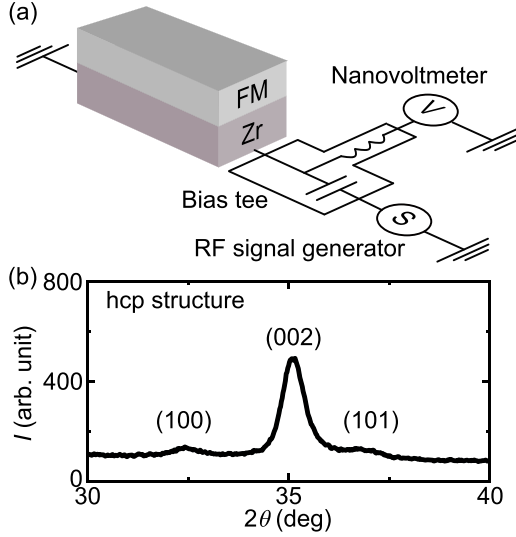


FIG. 1. (a) Schematic illustration of the ST-FMR for the FM/Zr bilayers. (b) An XRD pattern for a Zr(20 nm) single-layer film, where  $2\theta$  is the diffraction angle and  $I$  is the diffraction intensity. The XRD pattern shows that the Zr film is a hexagonal close-packed (hcp) structure.

signal-ground contact that guides an rf current into the device. Here, the number in parentheses represents the film thickness. During the ST-FMR measurement, an rf current was applied along the longitudinal direction of the device with a power of  $P = 100$  mW and a frequency of  $f$ . The rf current generates damping-like (DL) and field-like (FL) effective fields,  $H_{DL}$  and  $H_{FL}$ , as well as an Oersted field  $H_{Oe}$ . We also applied an in-plane external magnetic field  $H$  at an in-plane angle of  $\theta_H$ , where  $\theta_H$  is the angle between the magnetic field and the rf current. When  $f$  and  $H$  satisfy the FMR condition, the DL, FL, and Oersted fields drive a precession of the magnetization in the FM layer, which induces an oscillation of the device resistance through the anisotropic magnetoresistance (AMR). The oscillating resistance mixes with the rf current, yielding a direct current (dc) mixing voltage,  $V_{dc}$ . We measured  $V_{dc}$  using a bias tee and a nanovoltmeter at room temperature.

### III. RESULTS AND DISCUSSION

Figure 2(a) shows ST-FMR spectra for the Ni(6 nm)/Zr(12 nm) and the  $\text{Ni}_{81}\text{Fe}_{19}$ (6 nm)/Zr(12 nm) bilayers at  $\theta_H = 45^\circ$ , respectively. The measured  $V_{dc}$  signals are consistent with the prediction of the ST-FMR [19]:

$$V_{dc} = V_{\text{sym}} \frac{W^2}{(\mu_0 H - \mu_0 H_{\text{res}})^2 + W^2} + V_{\text{asym}} \frac{W(\mu_0 H - \mu_0 H_{\text{res}})}{(\mu_0 H - \mu_0 H_{\text{res}})^2 + W^2}, \quad (1)$$

where  $H_{\text{res}}$  is the FMR field,  $W$  is the linewidth, and  $\mu_0$  is the vacuum permeability. Here, the symmetric component  $V_{\text{sym}}$  is proportional to  $H_{DL}$ , while the antisymmetric component  $V_{\text{asym}}$  is proportional to the sum of  $H_{FL}$  and  $H_{Oe}$ . As shown in Fig. 2(b),  $V_{\text{sym}}$  and  $V_{\text{asym}}$  are proportional to  $\sin 2\theta_H \cos \theta_H$  in both Ni/Zr and  $\text{Ni}_{81}\text{Fe}_{19}$ /Zr bilayers, which is consistent with the prediction of the ST-FMR [20]. This result indicates

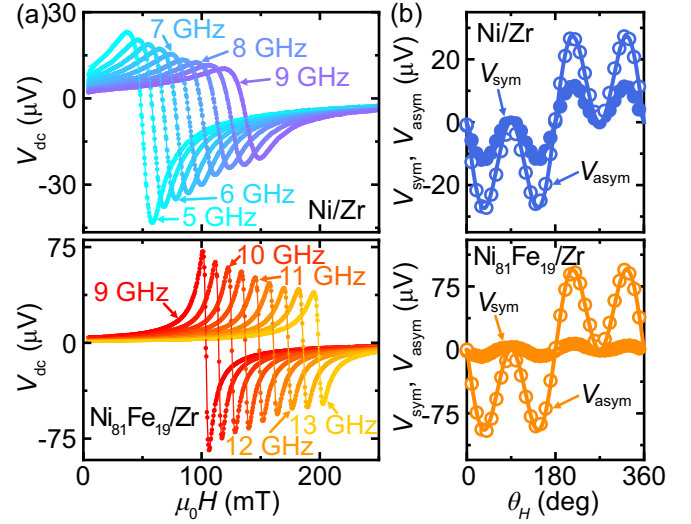


FIG. 2. (a) ST-FMR spectra for the Ni(6 nm)/Zr(12 nm) bilayer (upper) and for the  $\text{Ni}_{81}\text{Fe}_{19}$ (6 nm)/Zr(12 nm) bilayer (lower) at various frequencies  $f$ . (b) In-plane magnetic field angle  $\theta_H$  dependence of the symmetric  $V_{\text{sym}}$  and antisymmetric  $V_{\text{asym}}$  components of the  $V_{dc}$  signal for the Ni(6 nm)/Zr(12 nm) bilayer at  $f = 9$  GHz (upper) and for the  $\text{Ni}_{81}\text{Fe}_{19}$ (6 nm)/Zr(12 nm) bilayer at  $f = 13$  GHz (lower). The solid and open circles are the experimental data of  $V_{\text{sym}}$  and  $V_{\text{asym}}$ , respectively. The solid curves are the fitting results using functions proportional to  $\sin 2\theta_H \cos \theta_H$ .

that an out-of-plane Oersted field is negligible in the observed voltage, indicating that the rf current flow is uniform in the ST-FMR devices.

From the measured signals, we determine the DL torque efficiency per applied electric field, defined as [21]

$$\xi_{DL}^E = \frac{2e}{\hbar} \mu_0 M_s t_{\text{FM}} \frac{H_{DL}}{E}, \quad (2)$$

where  $\hbar$  is the reduced Planck constant,  $M_s$  is the saturation magnetization,  $t_{\text{FM}}$  is thickness of the FM layer, and  $E$  is the applied electric field. The DL effective field  $H_{DL}$  can be determined from the magnitude of the symmetric component  $V_{\text{sym}}$  of the ST-FMR signal at  $\theta_H = 45^\circ$  using [20]

$$\mu_0 H_{DL} = \frac{2\sqrt{2}V_{\text{sym}}W}{I_{\text{rf}}\Delta R_{\text{AMR}}} \frac{2\mu_0 H_{\text{res}} + \mu_0 M_{\text{eff}}}{\mu_0 H_{\text{res}} + \mu_0 M_{\text{eff}}} \sqrt{1 + \frac{\mu_0 M_{\text{eff}}}{\mu_0 H_{\text{res}}}}, \quad (3)$$

where  $I_{\text{rf}}$  is the rf current flowing in the device and  $\Delta R_{\text{AMR}}$  is the resistance change of the device due to the AMR. In Fig. 3(a), we show in-plane magnetic field angle  $\theta_H$  dependence of the resistance  $R$  of the Ni(6 nm)/Zr(12 nm) bilayer. By fitting the  $\theta_H$  dependence of  $R$  using  $R = R_0 + \Delta R_{\text{AMR}} \cos^2 \theta_H$ , we obtain  $\Delta R_{\text{AMR}}$ , where  $R_0$  represents the device resistance at  $\theta_H = 90^\circ$ . The rf current flowing in the device,  $I_{\text{rf}}$ , can be estimated by measuring the transmission and reflection coefficients of the ST-FMR device using a vector network analyzer or by observing the resistance change caused by the application of the rf current due to the Joule heating [20,22–25]. In this study we use the Joule heating of the device as a calibration [20,24,25]. In Figs. 3(b) and 3(c), we show resistance change  $\Delta R$  induced by applying an rf current with a power of  $P$  and a dc current  $I_{dc}$ , respectively.

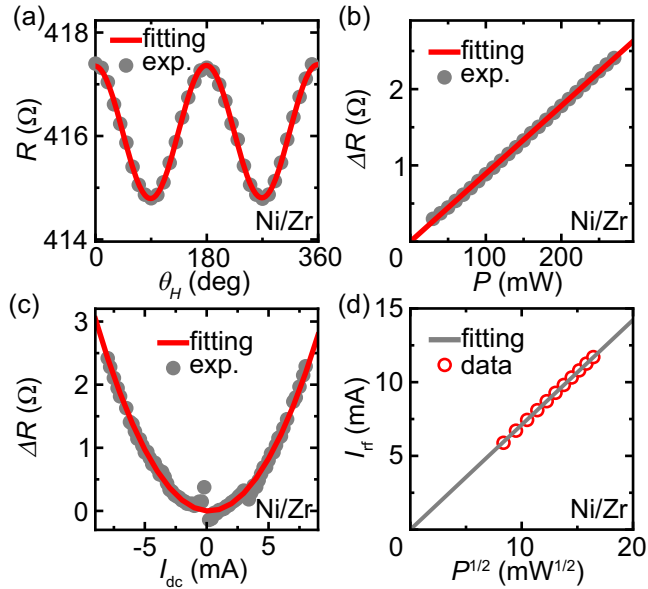


FIG. 3. (a) In-plane magnetic field angle  $\theta_H$  dependence of the device resistance  $R$  for the Ni(6 nm)/Zr(12 nm) bilayer. (b) rf power  $P$  dependence of  $\Delta R = R(P) - R(P = 0)$  for the Ni(6 nm)/Zr(12 nm) bilayer at  $f = 9$  GHz, where  $R(P)$  is the device resistance measured with applying an rf current with a power of  $P$ . (c) dc current  $I_{dc}$  dependence of  $\Delta R = R(I_{dc}) - R(I_{dc} = 0)$  for the Ni(6 nm)/Zr(12 nm) bilayer, where  $R(I_{dc})$  is the device resistance measured with applying a dc current  $I_{dc}$ . (d) The relation between  $\sqrt{P}$  and the rf current  $I_{rf}$  flowing in the Ni(6 nm)/Zr(12 nm) bilayer device, estimated from the results shown in (b) and (c). The solid circles in gray in (a)–(c) are the experimental data. The solid curves and lines are the fitting results. The open circles in red in (d) are the estimated relation between  $\sqrt{P}$  and  $I_{rf}$ .

When the rf or dc current is applied, the resistance  $R$  of the device increases as a result of the Joule heating. Figures 3(b) and 3(c) show that the resistance change  $\Delta R$  is linear to  $P$  and follows the parabolic relationship to  $I_{dc}$ ,  $\Delta R(P) = aP$  and  $\Delta R(I_{dc}) = bI_{dc}^2$ , as expected from the sample heating. From this result we can estimate the relation between the applied power  $P$  and the rf current  $I_{rf}$  flowing in the device using  $I_{rf} = \sqrt{(2a/b)P}$ , where we used the fact that the sample heating is proportional to  $RI_{dc}^2$  for the application of the dc current, whereas it is proportional to  $RI_{rf}^2/2$  for the application of the continuous rf current in the form of  $I_{rf} \cos 2\pi ft$ . Figure 3(d) shows the relation between  $\sqrt{P}$  and  $I_{rf}$ , estimated from the result shown in Figs. 3(b) and 3(c). We determined  $R_0$ ,  $\Delta R_{AMR}$ , and  $I_{rf}$  for all the devices used in the present work as shown in Figs. 4(a)–4(c). From the obtained values with  $E = R_0 I_{rf}/d$ , we obtain the applied electric field  $E$  as shown in Fig. 4(d), where  $d$  is the distance between the electrodes.

Figure 5(a) shows Zr-layer thickness  $t_{Zr}$  dependence of the DL torque efficiency  $\xi_{DL}^E$  for the Ni/Zr and Ni<sub>81</sub>Fe<sub>19</sub>/Zr bilayers, obtained from the ST-FMR result using Eq. (2). This result shows that  $\xi_{DL}^E$  increases with increasing the Zr-layer thickness  $t_{Zr}$ . Here, the  $t_{Zr}$ -dependent variation in  $\xi_{DL}^E$  cannot be attributed to a possible change in the magnetic properties of the FM layer; in the FM/Zr bilayers, the effective demagnetization field  $M_{eff}$  is almost independent of  $t_{Zr}$ , as shown

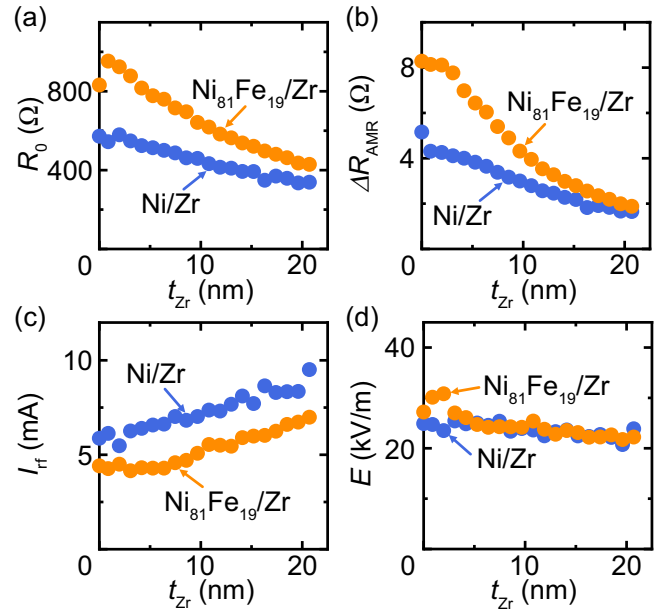


FIG. 4. Zr-layer thickness  $t_{Zr}$  dependence of (a) the resistance  $R_0$  and (b) the resistance change due to the AMR  $\Delta R_{AMR}$  for the Ni<sub>81</sub>Fe<sub>19</sub>(6 nm)/Zr( $t_{Zr}$ ) (orange) and Ni(6 nm)/Zr( $t_{Zr}$ ) (blue) bilayers.  $t_{Zr}$  dependence of (c) the rf current flowing in the device  $I_{rf}$  at  $P = 100$  mW and (d) the applied electric field  $E$  for the Ni<sub>81</sub>Fe<sub>19</sub>(6 nm)/Zr( $t_{Zr}$ ) at  $f = 13$  GHz (orange) and Ni(6 nm)/Zr( $t_{Zr}$ ) at  $f = 9$  GHz (blue) bilayers.

in Fig. 5(b). We also note that the electronic properties of the Zr layer are also independent of  $t_{Zr}$ . In fact, as shown in Fig. 5(c),  $t_{Zr}$  dependence of the resistivity  $\rho$  of the Zr layer is consistent with  $\rho(t_{Zr}) = at_{Zr}^{-1} + \rho_{bulk}$ , demonstrating that the bulk resistivity  $\rho_{bulk}$  is unchanged by changing  $t_{Zr}$ , where  $at_{Zr}^{-1}$  arises from the surface scattering. These results indicate that the  $t_{Zr}$ -dependent DL torque originates from the bulk effects, the SHE or OHE, in the Zr layer.

We note that as shown in Fig. 5(a), the sign of  $\xi_{DL}^E$  is positive, which is opposite to the prediction of the DL torque due to the SHE, because the sign of the spin Hall conductivity of Zr is negative:  $\sigma_{SH} = -170 (\hbar/e)(\Omega \text{ cm})^{-1}$  [13]. This clearly shows that the SHE in the Zr layer is not the main source of the observed DL torque. In fact, the observed features of  $\xi_{DL}^E$  are consistent with those expected from the orbital torque due to the OHE in the Zr layer. First, the sign of  $\xi_{DL}^E$  is consistent with the positive orbital Hall conductivity of Zr [12,13]. Second,  $\xi_{DL}^E$  does not saturate in the investigated  $t_{Zr}$  range, despite the short spin diffusion length in Zr:  $\lambda_s = 3.1$  nm [13]. The  $t_{Zr}$  dependence of  $\xi_{DL}^E$  is consistent with that expected from the orbital torque, because the orbital diffusion length has been found to be longer than the spin diffusion length [15,17]. Third,  $\xi_{DL}^E$  in the Ni/Zr bilayer is larger than that in the Ni<sub>81</sub>Fe<sub>19</sub>/Zr bilayer. Since orbital currents interact with the magnetization through the spin-orbit interaction, the orbital torque is quite sensitive to the electronic structure of the FM layer [11]. Among the conventional 3d FMs, Ni is predicted to show the strongest orbital response [14]. The strong orbital response in Ni originates from the optimal electron occupation of  $d$  orbital shells such that the Fermi energy is located in

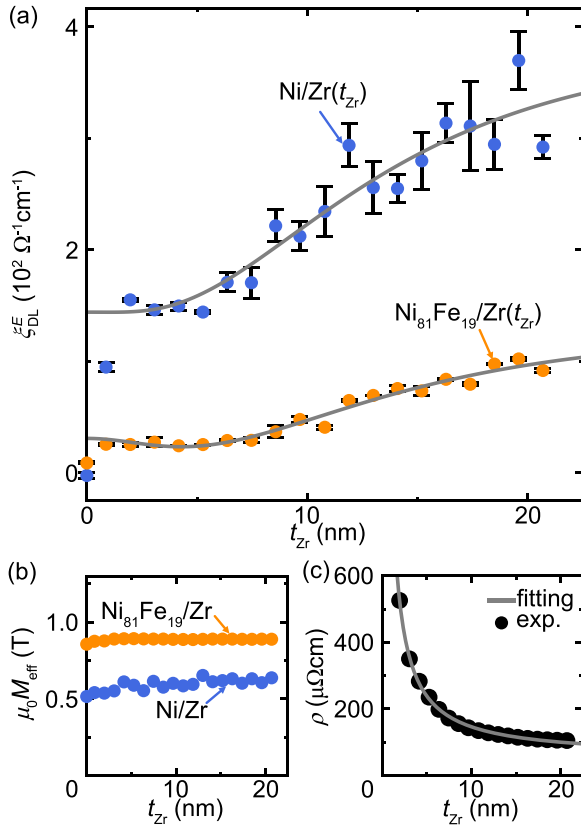


FIG. 5. (a) Zr-layer thickness  $t_{\text{Zr}}$  dependence of the DL torque efficiency  $\xi_{\text{DL}}^E$  for the Ni<sub>81</sub>Fe<sub>19</sub>(6 nm)/Zr( $t_{\text{Zr}}$ ) (orange) and Ni(6 nm)/Zr( $t_{\text{Zr}}$ ) (blue) bilayers. The solid circles are the experimental data, and the solid curves are the fitting results. The error bars are the standard deviation of the measurements at different  $f$ . (b)  $t_{\text{Zr}}$  dependence of the effective demagnetization  $M_{\text{eff}}$  of the Ni<sub>81</sub>Fe<sub>19</sub>(6 nm)/Zr( $t_{\text{Zr}}$ ) (orange) and Ni(6 nm)/Zr( $t_{\text{Zr}}$ ) (blue) bilayers. (c)  $t_{\text{Zr}}$  dependence of the electric resistivity  $\rho$  of the Zr layer. The solid circles in black are the experimental data, and the solid curve in gray represents the fitting result using  $\rho(t_{\text{Zr}}) = at_{\text{Zr}}^{-1} + \rho_{\text{bulk}}$ , where  $\rho_{\text{bulk}} = 53.4 \pm 1.7 \mu\Omega\text{cm}$ .

the energy where the spin-orbit correlation is strong [14,17]. This implies that the orbital response can be strongly affected by the change of the electronic occupation by Fe doping. Although there is no direct calculation for the spin-orbit correlation in Ni<sub>81</sub>Fe<sub>19</sub>, a recent experiment has demonstrated that the orbital response in Ni<sub>81</sub>Fe<sub>19</sub> is clearly weaker than that in Ni in FM/Ti and FM/W bilayers [17]. Thus the larger torque efficiency in the Ni/Zr bilayer also supports that orbital currents are responsible for the observed torque. These results demonstrate that the current-induced torque in the FM/Zr bilayers is dominated by the orbital torque originating from the OHE in the Zr layer.

The interpretation of the orbital-dominated torque in the Zr-based structures is further supported by Ni-layer thickness  $t_{\text{Ni}}$  dependence of  $\xi_{\text{DL}}^E$ . In the FM/Zr bilayer, spin currents injected into the FM layer rapidly oscillate and decay by spin dephasing. Due to the short spin dephasing length, the DL effective field due to the SHE varies as  $H_{\text{DL}} \propto 1/t_{\text{FM}}$ , and hence the spin torque efficiency is independent of  $t_{\text{FM}}$ . In contrast, orbital currents injected into the FM layer can

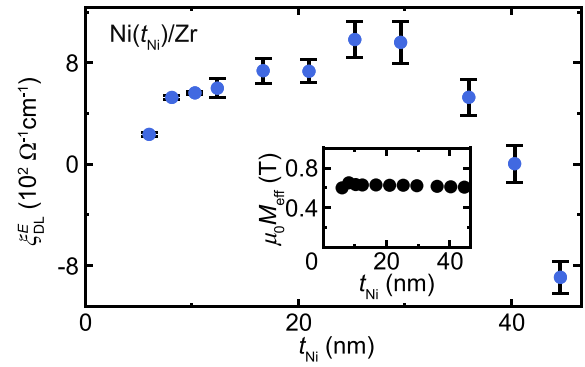


FIG. 6. Ni-layer thickness  $t_{\text{Ni}}$  dependence of the DL torque efficiency  $\xi_{\text{DL}}^E$ . The inset shows the effective demagnetization field  $M_{\text{eff}}$  for the Ni( $t_{\text{Ni}}$ )/Zr(10 nm) bilayer.

travel much longer distances than the spin dephasing length without oscillation through the degenerate orbital hot spots in the momentum space [26]. The semirealistic calculations predict a monotonic increase of the orbital torque efficiency with  $t_{\text{FM}}$  as a result of the long-range orbital transport [26], which has been confirmed experimentally [17]. To test the role of the spin and orbital currents in generating the DL torque, we measured  $t_{\text{Ni}}$  dependence of  $\xi_{\text{DL}}^E$  for the Ni( $t_{\text{Ni}}$ )/Zr(10 nm) bilayer, as shown in Fig. 6. Figure 6 shows that  $\xi_{\text{DL}}^E$  increases with  $t_{\text{Ni}}$  at  $t_{\text{Ni}} < 30$  nm despite the fact that the magnetic properties of the Ni layer are almost unchanged in this  $t_{\text{Ni}}$  range, as evidenced by a negligible change in  $M_{\text{eff}}$  (see the inset to Fig. 6). The monotonic increase in  $\xi_{\text{DL}}^E$  with  $t_{\text{Ni}}$  when  $t_{\text{Ni}} < 30$  nm in the Ni/Zr bilayer is consistent with the theoretical prediction, supporting that the OHE is the dominant mechanism of the observed DL torque. Here, a variation in the DL torque efficiency with the FM-layer thickness has also been reported in Co-based devices, where the SHE is the primary mechanism and the OHE is an additional contribution to the DL torque [18].

As shown in Fig. 6, by further increasing  $t_{\text{Ni}}$ ,  $\xi_{\text{DL}}^E$  decreases and becomes negative at  $t_{\text{Ni}} > 40$  nm, although the orbital torque is expected to be saturated with increasing  $t_{\text{Ni}}$ . This result indicates that an additional torque appears by increasing  $t_{\text{Ni}}$ , which can be attributed to a self-induced torque generated in the Ni layer. The self-induced torque originates from a spin accumulation generated in the Ni layer and the asymmetry between the top SiO<sub>2</sub>/Ni and bottom Ni/Zr interfaces [27]. This torque depends on the FM-layer thickness and can be sizable only when the FM layer is thicker than the exchange length [27]. We have provided evidence for large self-induced torques with a negative sign in thick Ni single layers without a Zr layer in our previous work [17]. The result shows that the self-induced torque in a Ni film is non-negligible only when  $t_{\text{Ni}} > 10$  nm, implying that the DL torque efficiency in the Ni/Zr bilayer is affected by the self-induced torque in the Ni layer when  $t_{\text{Ni}} > 10$  nm. By further increasing  $t_{\text{Ni}}$ , the self-induced torque with a negative sign increases and becomes sizable, especially at  $t_{\text{Ni}} > 20$  nm [17]. In contrast, the orbital torque with a positive sign tends to saturate with increasing  $t_{\text{Ni}}$  [26]. Because of the different  $t_{\text{Ni}}$  dependences between the self-induced torque and orbital torque, their relative contribution to the DL torque changes with  $t_{\text{Ni}}$ , resulting

in the suppression of the observed orbital torque efficiency at  $t_{\text{Ni}} > 30$  nm. Thus the observed nonmonotonic change in the DL torque efficiency with  $t_{\text{Ni}}$ , shown in Fig. 6, can be attributed to the competition between the orbital torque with a positive sign and self-induced torque with a negative sign, supporting that the observed positive  $\xi_{\text{DL}}^E$  can be attributed to the orbital torque in the Ni/Zr bilayers.

Finally, we extract spin and orbital transport parameters by fitting the  $t_{\text{Zr}}$  dependence of the DL torque efficiency, shown in Fig. 5(a). We assume that the observed torque efficiency  $\xi_{\text{DL}}^E$  can be decomposed into a sum of three contributions as

$$\xi_{\text{DL}}^E = \sigma_{\text{SHE}}\delta_s \left[ 1 - \operatorname{sech}\left(\frac{t_{\text{Zr}}}{\lambda_s}\right) \right] + \eta_{\text{FM}}\sigma_{\text{OHE}}\delta_o \left[ 1 - \operatorname{sech}\left(\frac{t_{\text{Zr}}}{\lambda_o}\right) \right] + C. \quad (4)$$

In Eq. (4), the first term represents the DL torque efficiency due to the SHE, where  $\sigma_{\text{SHE}} (< 0)$  and  $\lambda_s$  are the spin Hall conductivity and spin diffusion length in the Zr layer, respectively [19].  $\delta_s$  characterizes the interface spin loss. By analogy with the spin torque efficiency, we assume that the DL torque efficiency due to the OHE varies with  $t_{\text{Zr}}$  as the second term in Eq. (4), where  $\sigma_{\text{OHE}} (> 0)$  and  $\lambda_o$  denote the orbital Hall conductivity and orbital diffusion length in the Zr layer, respectively. Here,  $\eta_{\text{FM}}$  represents the effective coupling between the orbital Hall currents and magnetization due to the spin-orbit correlation and spin exchange coupling in the FM layer [14,17].  $\delta_o$  characterizes the interface orbital loss. We assume  $\sigma_{\text{SHE}}$  and  $\sigma_{\text{OHE}}$  are independent of  $t_{\text{Zr}}$ . The third term,  $C$ , in Eq. (4) is a constant, which describes  $t_{\text{Zr}}$ -independent DL torque efficiency. This contribution can be attributed to interfacial spin-orbit torques. For the fitting using Eq. (4), we excluded the data at  $t_{\text{Zr}} < 1$  nm because the Zr layer is probably not continuous in this thickness range.

In Fig. 5(a) we show the fitting results. For the  $\text{Ni}_{81}\text{Fe}_{19}/\text{Zr}$  bilayer, the measured  $t_{\text{Zr}}$  dependence of  $\xi_{\text{DL}}^E$  is well fitted by Eq. (4). The extracted parameters are  $\sigma_{\text{SHE}}\delta_s = -57.8 \pm 13.6$  ( $\hbar/e$ ) $\Omega^{-1}\text{cm}^{-1}$ ,  $\lambda_s = 3.68 \pm 1.17$  nm,  $\eta_{\text{FM}}\sigma_{\text{OHE}}\delta_o = 152 \pm 14$  ( $\hbar/e$ ) $\Omega^{-1}\text{cm}^{-1}$ ,  $\lambda_o = 8.49 \pm 2.68$  nm, and  $C = 30.5 \pm 6.8$   $\Omega^{-1}\text{cm}^{-1}$ . The extracted values of  $\sigma_{\text{SHE}}$  and  $\lambda_s$  are reasonable for the spin Hall conductivity and spin diffusion length of Zr (see also Appendix) [12,13]. The large error in the extracted values of  $\sigma_{\text{SHE}}\delta_s$  and  $\lambda_s$  arises from the fact that the SHE contribution with a negative sign is not clear in the measured  $t_{\text{Zr}}$  dependence of  $\xi_{\text{DL}}^E$ . When neglecting the SHE contribution, the first term in Eq. (4), we obtain  $\eta_{\text{FM}}\sigma_{\text{OHE}}\delta_o = 147 \pm 9$  ( $\hbar/e$ ) $\Omega^{-1}\text{cm}^{-1}$ ,  $\lambda_o = 14.2 \pm 0.8$  nm,  $C = 18.1 \pm 6.4$   $\Omega^{-1}\text{cm}^{-1}$ . These results demonstrate that the orbital diffusion length is longer than the spin diffusion length, consistent with previous reports [15,17]. Using the extracted values of  $\lambda_s$  and  $\lambda_o$ , we also fitted the  $t_{\text{Zr}}$  dependence of  $\xi_{\text{DL}}^E$  for the Ni/Zr bilayer using Eq. (4), as shown in Fig. 5(a). From the fitting we obtain  $\sigma_{\text{SHE}}\delta_s = -58.7 \pm 52.6$  ( $\hbar/e$ ) $\Omega^{-1}\text{cm}^{-1}$ ,  $\eta_{\text{FM}}\sigma_{\text{OHE}}\delta_o = 296 \pm 52$  ( $\hbar/e$ ) $\Omega^{-1}\text{cm}^{-1}$ , and  $C = 144 \pm 22$   $\Omega^{-1}\text{cm}^{-1}$ . When neglecting the SHE contribution without fixing  $\lambda_o$ , we obtain  $\eta_{\text{FM}}\sigma_{\text{OHE}}\delta_o = 260 \pm 44$  ( $\hbar/e$ ) $\Omega^{-1}\text{cm}^{-1}$ ,  $\lambda_o = 9.66 \pm 2.32$  nm,  $C = 129 \pm 15$   $\Omega^{-1}\text{cm}^{-1}$ . These results demonstrate that the DL torque due to the OHE exceeds that due to the

SHE in the Zr-based systems, and the OHE contribution is more pronounced in the Ni/Zr bilayers.

The extracted orbital torque efficiencies show that the difference in the orbital torque between the  $\text{Ni}_{81}\text{Fe}_{19}/\text{Zr}$  and Ni/Zr bilayers is less pronounced than that between  $\text{Ni}_{81}\text{Fe}_{19}/\text{Ti}$  and Ni/Ti bilayers [17]. In the Zr-based devices, the orbital torque efficiency in the Ni/Zr bilayer is two times larger than that in the  $\text{Ni}_{81}\text{Fe}_{19}/\text{Zr}$  bilayer, while in the Ti-based devices, the DL torque efficiency in Ni/Ti bilayers is an order of magnitude larger than that in  $\text{Ni}_{81}\text{Fe}_{19}/\text{Ti}$  bilayers [17]. The difference in the orbital torque efficiencies between the Zr-based and Ti-based devices indicates that the orbital transparency at the FM/NM interface is sensitive to the materials combinations of the FM and NM layers. In particular, although the orbital Hall conductivity is comparable between Zr and Ti [12],  $\sigma_{\text{OHE}} \simeq 4000$  ( $\hbar/e$ ) $\Omega^{-1}\text{cm}^{-1}$ , the orbital torque efficiency  $\xi_{\text{DL,OHE}}^E$  is clearly different between the Ni/Zr and Ni/Ti bilayers;  $\xi_{\text{DL,OHE}}^E \simeq 400$   $\Omega^{-1}\text{cm}^{-1}$  in the Ni(6 nm)/Ti(8 nm) bilayer and  $\xi_{\text{DL,OHE}}^E \simeq \xi_{\text{DL}}^E - C \simeq 100$   $\Omega^{-1}\text{cm}^{-1}$  in the Ni(6 nm)/Zr(8 nm) bilayer. This result suggests that the orbital loss  $\delta_o$  at the Ni/Ti interface is lower than that at the Ni/Zr interface, and the orbital transparency at the Ni/Ti interface is higher than that at the Ni/Zr interface.

#### IV. CONCLUSIONS

In summary, we have investigated the current-induced torque generated in the  $\text{Ni}_{81}\text{Fe}_{19}/\text{Zr}$  and Ni/Zr bilayers. By varying the thickness of the Zr layer,  $t_{\text{Zr}}$ , we found that the DL torque with a positive sign increases with  $t_{\text{Zr}}$  both in the  $\text{Ni}_{81}\text{Fe}_{19}/\text{Zr}$  and Ni/Zr bilayers. The  $t_{\text{Zr}}$ -dependent positive DL torque has been attributed to the orbital torque generated by the OHE in the Zr layer. The orbital-dominated torque is supported by the Ni-layer thickness dependence of the torque efficiency.

The observed  $t_{\text{Zr}}$  dependence of the DL torque efficiency in the  $\text{Ni}_{81}\text{Fe}_{19}/\text{Zr}$  and Ni/Zr bilayers is different from that in CoFeB/Zr bilayers, reported previously, where the sign of the DL torque changes from positive to negative with increasing  $t_{\text{Zr}}$  [13]. A similar thickness-dependent change in the sign of the DL torque has been observed in heavy-metal/FM bilayers, such as Hf/CoFeB and Ta/CoFeB bilayers [28,29]. In these systems the sign reversal of the DL torque has been attributed to the competition between the SHE and interfacial Rashba effect. In contrast, in the CoFeB/Zr bilayer it is assumed that the interfacial Rashba spin-orbit coupling plays a minor role in generating the DL torque, as suggested by the negligible interfacial Dzyaloshinskii-Moriya interaction. Under this assumption the positive DL torque in the thin CoFeB/Zr devices has been discussed in terms of the orbital torque due to the OHE in the Zr layer, while the negative DL torque in the thick CoFeB/Zr devices has been attributed to the SHE. However, the relation between the interfacial Dzyaloshinskii-Moriya interaction and interfacial spin-orbit torques is nontrivial. We also note that the interfacial spin-orbit torque can be sizable even in the absence of heavy metals [30]. Our results for the  $\text{Ni}_{81}\text{Fe}_{19}/\text{Zr}$  and Ni/Zr bilayers suggest that interfacial spin-orbit torques cannot be neglected in FM/Zr devices, implying that the positive DL torque observed for the thin CoFeB/Zr

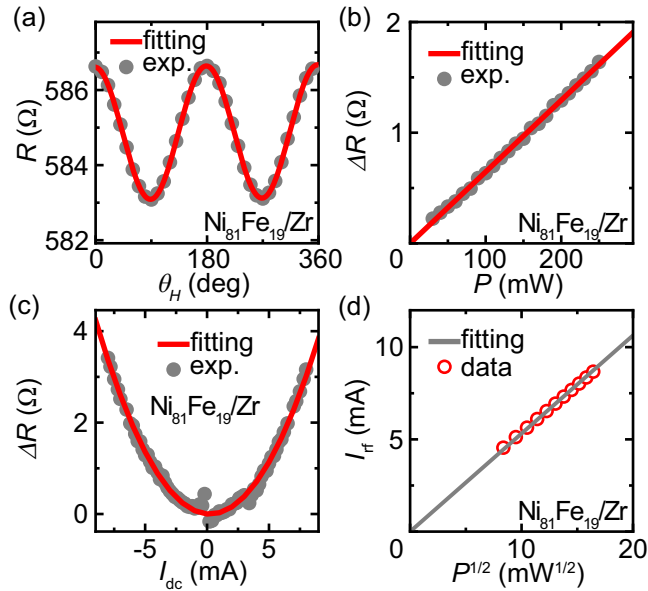


FIG. 7. (a)  $\theta_H$  dependence of the device resistance  $R$  for the  $\text{Ni}_{81}\text{Fe}_{19}(6 \text{ nm})/\text{Zr}(12 \text{ nm})$  bilayer. (b)  $P$  dependence of  $\Delta R = R(P) - R(P = 0)$  for the  $\text{Ni}_{81}\text{Fe}_{19}(6 \text{ nm})/\text{Zr}(12 \text{ nm})$  bilayer at  $f = 13 \text{ GHz}$ . (c)  $I_{dc}$  dependence of  $\Delta R = R(I_{dc}) - R(I_{dc} = 0)$  for the  $\text{Ni}_{81}\text{Fe}_{19}(6 \text{ nm})/\text{Zr}(12 \text{ nm})$  bilayer. (d) The relation between  $\sqrt{P}$  and  $I_{rf}$  flowing in the  $\text{Ni}_{81}\text{Fe}_{19}(6 \text{ nm})/\text{Zr}(12 \text{ nm})$  bilayer device, estimated from the results shown in (b) and (c). The solid circles in gray in (a)–(c) are the experimental data. The solid curves and lines are the fitting results. The open circles in red in (d) are the estimated relation between  $\sqrt{P}$  and  $I_{rf}$ .

bilayer can be attributed to the interfacial contribution. Our results also indicate that the orbital torque with a positive sign is pronounced in the FM/Zr devices with large  $t_{\text{Zr}}$  because the orbital diffusion length is longer than the spin diffusion length. The difference in the sign of the DL torque at large  $t_{\text{Zr}}$  between the FM/Zr bilayers suggests that the orbital response in the Ni/Zr and  $\text{Ni}_{81}\text{Fe}_{19}/\text{Zr}$  bilayers is stronger than that in the CoFeB/Zr bilayer. The observation of the orbital-dominated torque in the  $4d$ -metal devices provides important information for understanding angular momentum transport and dynamics in solid-state devices.

#### ACKNOWLEDGMENTS

We acknowledge fruitful discussions with Hyun-Woo Lee. This work was supported by JSPS KAKENHI (Grants No. 22H04964, No. 20H00337, and No. 20H02593), Spintronics Research Network of Japan (Spin-RNJ), and the MEXT Initiative to Establish Next-Generation Novel Integrated Circuits Centers (X-NICS) (Grant No. JPJ011438).

#### APPENDIX A

For the  $\text{Ni}_{81}\text{Fe}_{19}(6 \text{ nm})/\text{Zr}(12 \text{ nm})$  bilayer, we show  $\theta_H$  dependence of  $R$  in Fig. 7(a). We also show  $P$  and  $I_{dc}$  depen-

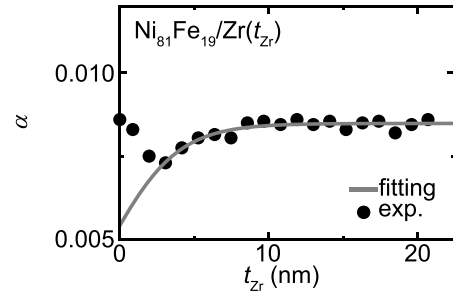


FIG. 8. Zr-layer thickness  $t_{\text{Zr}}$  dependence of the magnetic damping  $\alpha$  for the  $\text{Ni}_{81}\text{Fe}_{19}(6 \text{ nm})/\text{Zr}(t_{\text{Zr}})$  bilayer. The solid circles are the experimental data, and the solid curve is the fitting result. For the fitting, the data around  $t_{\text{Zr}} = 0 \text{ nm}$  are excluded, the same as in the fitting of the  $t_{\text{Zr}}$  dependence of  $\xi_{\text{DL}}^E$ , shown in Fig. 5(a), because the Zr layer is probably not continuous.

dences of  $\Delta R$  in Figs. 7(b) and 7(c), respectively. From these results we determined the relation between  $\sqrt{P}$  and  $I_{rf}$  for the  $\text{Ni}_{81}\text{Fe}_{19}/\text{Zr}$  bilayer, as shown in Fig. 7(d).

#### APPENDIX B

We estimate the spin diffusion length in the Zr layer from Zr-layer thickness  $t_{\text{Zr}}$  dependence of the magnetic damping constant  $\alpha$  for the  $\text{Ni}_{81}\text{Fe}_{19}(6 \text{ nm})/\text{Zr}(t_{\text{Zr}})$  bilayer, shown in Fig. 8. The magnetic damping constant  $\alpha$  was determined by fitting frequency  $f$  dependence of the ST-FMR spectral width  $W$  using  $W = (2\pi\alpha/\gamma)f + W_{\text{ext}}$ , where  $W_{\text{ext}}$  is the inhomogeneous linewidth broadening of the extrinsic contribution. Figure 8 shows that  $\alpha$  increases with  $t_{\text{Zr}}$  and saturates at  $t_{\text{Zr}} > 10 \text{ nm}$ , except for a few plots around  $t_{\text{Zr}} = 0 \text{ nm}$ , where the Zr layer is probably not continuous.

The enhancement of  $\alpha$  with increasing  $t_{\text{Zr}}$  can be attributed to the spin pumping [31]. The damping enhancement due to the spin pumping is expressed as [31]

$$\alpha(t_{\text{Zr}}) = \alpha_0 + \frac{\gamma \hbar}{4\pi M_s t_{\text{FM}}} g_{\text{eff}}^{\uparrow\downarrow}(t_{\text{Zr}}), \quad (\text{B1})$$

where  $\alpha_0$  is the intrinsic magnetic damping of the  $\text{Ni}_{81}\text{Fe}_{19}$  layer and  $\gamma$  is the gyromagnetic ratio.

$$g_{\text{eff}}^{\uparrow\downarrow}(t_{\text{Zr}}) = \frac{g^{\uparrow\downarrow}}{1 + (2\sqrt{\varepsilon}/3 \tanh(t_{\text{Zr}}/\lambda_s))^{-1}} \quad (\text{B2})$$

is the effective spin-mixing conductance, where  $g^{\uparrow\downarrow}$  is the spin-mixing conductance and  $\varepsilon$  is the ratio of the momentum to spin-flip scattering time. By fitting the  $t_{\text{Zr}}$  dependence of  $\alpha$  except for the data around  $t_{\text{Zr}} = 0 \text{ nm}$  using Eqs. (B1) and (B2), we obtain  $\varepsilon = 0.0117 \pm 0.0051$  and the spin diffusion length of the Zr layer as  $\lambda_s = 4.50 \pm 0.76 \text{ nm}$ .

[1] A. Hoffmann, Spin Hall effects in metals, *IEEE Trans. Magn.* **49**, 5172 (2013).

[2] J. Sinova, S. O. Valenzuela, J. Wunderlich, C. H. Back, and T. Jungwirth, Spin Hall effects, *Rev. Mod. Phys.* **87**, 1213 (2015).

- [3] A. Manchon, J. Železný, I. M. Miron, T. Jungwirth, J. Sinova, A. Thiaville, K. Garello, and P. Gambardella, Current-induced spin-orbit torques in ferromagnetic and antiferromagnetic systems, *Rev. Mod. Phys.* **91**, 035004 (2019).
- [4] J. Ryu, S. Lee, K.-J. Lee, and B.-G. Park, Current-induced spin-orbit torques for spintronic applications, *Adv. Mater.* **32**, 1907148 (2020).
- [5] B. A. Bernevig, T. L. Hughes, and S. C. Zhang, Orbitoronics: The Intrinsic Orbital Current in *p*-Doped Silicon, *Phys. Rev. Lett.* **95**, 066601 (2005).
- [6] T. Tanaka, H. Kontani, M. Naito, T. Naito, D. S. Hirashima, K. Yamada, and J. Inoue, Intrinsic spin Hall effect and orbital Hall effect in *4d* and *5d* transition metals, *Phys. Rev. B* **77**, 165117 (2008).
- [7] H. Kontani, T. Tanaka, D. S. Hirashima, K. Yamada, and J. Inoue, Giant Orbital Hall Effect in Transition Metals: Origin of Large Spin and Anomalous Hall Effects, *Phys. Rev. Lett.* **102**, 016601 (2009).
- [8] D. Go, D. Jo, C. Kim, and H.-W. Lee, Intrinsic Spin and Orbital Hall Effects from Orbital Texture, *Phys. Rev. Lett.* **121**, 086602 (2018).
- [9] D. Jo, D. Go, and H.-W. Lee, Gigantic intrinsic orbital Hall effects in weakly spin-orbit coupled metals, *Phys. Rev. B* **98**, 214405 (2018).
- [10] D. Go and H.-W. Lee, Orbital torque: Torque generation by orbital current injection, *Phys. Rev. Res.* **2**, 013177 (2020).
- [11] D. Go, F. Freimuth, J.-P. Hanke, F. Xue, O. Gomonay, K.-J. Lee, S. Blügel, P. M. Haney, H.-W. Lee, and Y. Mokrousov, Theory of current-induced angular momentum transfer dynamics in spin-orbit coupled systems, *Phys. Rev. Res.* **2**, 033401 (2020).
- [12] L. Salemi and P. M. Oppeneer, First-principles theory of intrinsic spin and orbital Hall and Nernst effects in metallic monoatomic crystals, *Phys. Rev. Mater.* **6**, 095001 (2022).
- [13] Z. C. Zheng, Q. X. Guo, D. Jo, D. Go, L. H. Wang, H. C. Chen, W. Yin, X. M. Wang, G. H. Yu, W. He, H.-W. Lee, J. Teng, and T. Zhu, Magnetization switching driven by current-induced torque from weakly spin-orbit coupled Zr, *Phys. Rev. Res.* **2**, 013127 (2020).
- [14] D. Lee, D. Go, H.-J. Park, W. Jeong, H.-W. Ko, D. Yun, D. Jo, S. Lee, G. Go, J. H. Oh, K.-J. Kim, B.-G. Park, B.-C. Min, H. C. Koo, H.-W. Lee, O. Lee, and K.-J. Lee, Orbital torque in magnetic bilayers, *Nat. Commun.* **12**, 6710 (2021).
- [15] S. Lee, M.-G. Kang, D. Go, D. Kim, J.-H. Kang, T. Lee, G.-H. Lee, J. Kang, N. J. Lee, Y. Mokrousov, S. Kim, K.-J. Kim, K.-J. Lee, and B.-G. Park, Efficient conversion of orbital Hall current to spin current for spin-orbit torque switching, *Commun. Phys.* **4**, 234 (2021).
- [16] Y.-G. Choi, D. Jo, K.-H. Ko, D. Go, K.-H. Kim, H. G. Park, C. Kim, B.-C. Min, G.-M. Choi, and H.-W. Lee, Observation of the orbital Hall effect in a light metal Ti, [arXiv:2109.14847](https://arxiv.org/abs/2109.14847).
- [17] H. Hayashi, D. Jo, D. Go, Y. Mokrousov, H.-W. Lee, and K. Ando, Observation of long-range orbital transport and giant orbital torque, *Commun. Phys.* **6**, 32 (2023).
- [18] G. Sala and P. Gambardella, Giant orbital Hall effect and orbital-to-spin conversion in *3d*, *5d*, and *4f* metallic heterostructures, *Phys. Rev. Res.* **4**, 033037 (2022).
- [19] L. Liu, T. Moriyama, D. C. Ralph, and R. A. Buhrman, Spin-Torque Ferromagnetic Resonance Induced by the Spin Hall Effect, *Phys. Rev. Lett.* **106**, 036601 (2011).
- [20] D. Fang, H. Kurebayashi, J. Wunderlich, K. Výborný, L. Zárbo, R. Campion, A. Casiraghi, B. Gallagher, T. Jungwirth, and A. Ferguson, Spin-orbit-driven ferromagnetic resonance, *Nat. Nanotechnol.* **6**, 413 (2011).
- [21] M.-H. Nguyen, D. C. Ralph, and R. A. Buhrman, Spin Torque Study of the Spin Hall Conductivity and Spin Diffusion Length in Platinum Thin Films with Varying Resistivity, *Phys. Rev. Lett.* **116**, 126601 (2016).
- [22] Y. Wang, P. Deorani, X. Qiu, J. H. Kwon, and H. Yang, Determination of intrinsic spin Hall angle in Pt, *Appl. Phys. Lett.* **105**, 152412 (2014).
- [23] Y. Wang, R. Ramaswamy, M. Motapothula, K. Narayanapillai, D. Zhu, J. Yu, T. Venkatesan, and H. Yang, Room-temperature giant charge-to-spin conversion at the SrTiO<sub>3</sub> – LaAlO<sub>3</sub> oxide interface, *Nano Lett.* **17**, 7659 (2017).
- [24] V. Tshitoyan, C. Ciccarelli, A. P. Mihai, M. Ali, A. C. Irvine, T. A. Moore, T. Jungwirth, and A. J. Ferguson, Electrical manipulation of ferromagnetic NiFe by antiferromagnetic IrMn, *Phys. Rev. B* **92**, 214406 (2015).
- [25] T. Gao, A. Qaiumzadeh, H. An, A. Musha, Y. Kageyama, J. Shi, and K. Ando, Intrinsic Spin-Orbit Torque Arising from the Berry Curvature in a Metallic-Magnet/Cu-Oxide Interface, *Phys. Rev. Lett.* **121**, 017202 (2018).
- [26] D. Go, D. Jo, K.-W. Kim, S. Lee, M.-G. Kang, B.-G. Park, S. Blügel, H.-W. Lee, and Y. Mokrousov, Long-range orbital magnetoelectric torque in ferromagnets, [arXiv:2106.07928](https://arxiv.org/abs/2106.07928).
- [27] W. Wang, T. Wang, V. P. Amin, Y. Wang, A. Radhakrishnan, A. Davidson, S. R. Allen, T. J. Silva, H. Ohldag, D. Balzar, B. L. Zink, P. M. Haney, J. Q. Xiao, D. G. Cahill, V. O. Lorenz, and X. Fan, Anomalous spin-orbit torques in magnetic single-layer films, *Nat. Nanotechnol.* **14**, 819 (2019).
- [28] R. Ramaswamy, X. Qiu, T. Dutta, S. D. Pollard, and H. Yang, Hf thickness dependence of spin-orbit torques in Hf/CoFeB/MgO heterostructures, *Appl. Phys. Lett.* **108**, 202406 (2016).
- [29] J. Kim, J. Sinha, M. Hayashi, M. Yamanouchi, S. Fukami, T. Suzuki, S. Mitani, and H. Ohno, Layer thickness dependence of the current-induced effective field vector in Ta|CoFeB|MgO, *Nat. Mater.* **12**, 240 (2013).
- [30] Y. Kageyama, Y. Tazaki, H. An, T. Harumoto, T. Gao, J. Shi, and K. Ando, Spin-orbit torque manipulated by fine-tuning of oxygen-induced orbital hybridization, *Sci. Adv.* **5**, eaax4278 (2019).
- [31] Y. Tserkovnyak, A. Brataas, G. E. Bauer, and B. I. Halperin, Nonlocal magnetization dynamics in ferromagnetic heterostructures, *Rev. Mod. Phys.* **77**, 1375 (2005).